Science
AAAS

Extremely Efficient Multiple Electron-Hole Pair Generation in Carbon Nanotube Photodiodes

Nathaniel M. Gabor, *et al.*

Science **325**, 1367 (2009);
DOI: 10.1126/science.1176112

Science (print ISSN 0036-8075; online ISSN 1095-9203) is published weekly, except the last week in December, by the American Association for the Advancement of Science, 1200 New York Avenue NW, Washington, DC 20005.

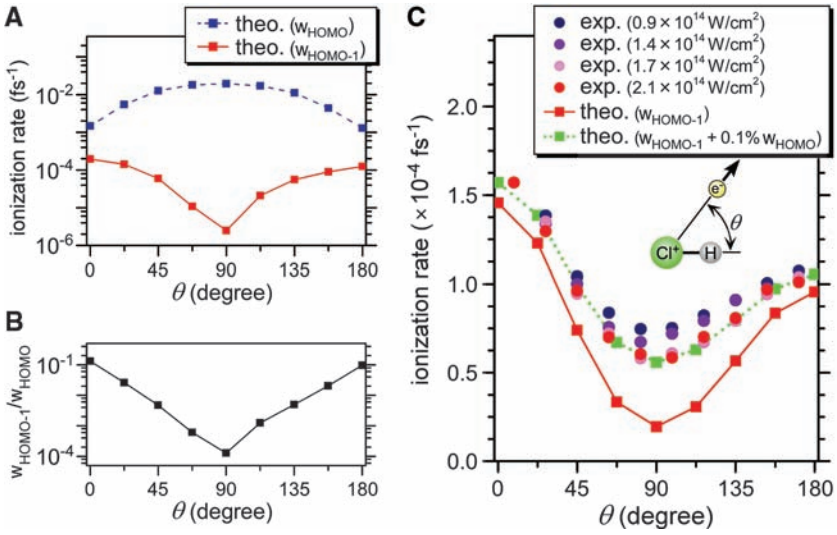

Fig. 4. (**A**) DFT calculated angular ionization probability of HOMO [$w_{HOMO}(\theta)$, dashed line] and HOMO-1 [$w_{HOMO-1}(\theta)$, solid line] at an intensity of 1.4×10^{14} W/cm^2. (**B**) Ratio w_{HOMO-1}/w_{HOMO} from (A). (**C**) Comparison of experiment and theory for the HCl angular ionization probability. The experimental curves are normalized to $\theta = 0°$. Solid line, calculated MFPAD of HOMO-1 convoluted with the experimental angular uncertainty (±30°); dotted line, same as solid line but including 0.1% of the HOMO angular distribution.

we measure the slit through which the electron passes, there can be no interference [except for a post-tunneling shake-up process (*4*) or the weak contribution through the X-A coupling]. However, in many experiments the tunneling orbital is not distinguishable. Electron wave packets must escape through the tunnel within a very restricted time window near each field maximum. Their coherent superposition will influence the angle-dependent rates. This kind of interference may be responsible for the very sharply peaked tunneling distribution found for CO_2 (*26*).

Second, ionization creates an electron and a correlated ion (*27*). Simultaneous tunneling from two or more orbitals locks the phase of the ion's states (*11*). Hence, a correlated bound electron wave packet is created in the ion that can be probed by the tunneled electron through recollision. This process is the analog to the creation of vibrational wave packets in molecules by tunneling (*28*, *29*). Whereas vibrational wave packets typically evolve on the femtosecond scale, bound electron wave packets exhibit true attosecond dynamics and are expected to be a ubiquitous feature of laser-driven tunneling in both molecular gases and solids (*14*).

Third, we have shown that tunneling selectively occurs with a specific orientation within a homogeneous sample. The only requirement for probing orbitals (and orbital dynamics) in two-color experiments (*30*, *31*) is that ionization labels the orbital. Our experiment shows that, in principle, molecules could be selected on the basis of their dipole moment.

References and Notes

1. P. Eckle *et al.*, *Science* **322**, 1525 (2008).
2. G. Binning, H. Rohrer, Ch. Gerber, E. Weibel, *Phys. Rev. Lett.* **49**, 57 (1982).
3. M. Meckel *et al.*, *Science* **320**, 1478 (2008).
4. I. V. Litvinyuk *et al.*, *Phys. Rev. Lett.* **94**, 033003 (2005).
5. W. A. Bryan *et al.*, *Nat. Phys.* **2**, 379 (2006).
6. T. Kanai, S. Minemoto, H. Sakai, *Nature* **435**, 470 (2005).
7. W. Li *et al.*, *Science* **322**, 1207 (2008); published online 29 October 2008 (10.1126/science.1163077).
8. X. Zhou *et al.*, *Phys. Rev. Lett.* **100**, 073902 (2008).
9. W. Boutu *et al.*, *Nat. Phys.* **4**, 545 (2008).
10. B. K. McFarland, J. P. Farrell, P. H. Bucksbaum, M. Gühr, *Science* **322**, 1232 (2008); published online 29 October 2008 (10.1126/science.1162780).
11. O. Smirnova *et al.*, *Nature* 10.1038/nature08253 (2009).
12. Y.J. Chen, J. Liu, B. Hu, *J. Chem. Phys.* **130**, 044311 (2009).
13. A.-T. Le, R. R. Lucchese, M. T. Lee, C. D. Lin, http://arxiv.org/abs/0901.1311 (2009).
14. M. Gertsvolf *et al.*, *Phys. Rev. Lett.* **101**, 243001 (2008).
15. P. H. Bucksbaum, A. Zavriyev, H. G. Muller, D. W. Schumacher, *Phys. Rev. Lett.* **64**, 1883 (1990).
16. A. Staudte *et al.*, *Phys. Rev. Lett.* **102**, 033004 (2009).
17. See supporting material on *Science* Online.
18. J. Ullrich *et al.*, *Rep. Prog. Phys.* **66**, 1463 (2003).
19. P. B. Corkum, N. H. Burnett, F. Brunel, *Phys. Rev. Lett.* **62**, 1259 (1989).
20. N. B. Delone, V. P. Krainov. *Phys. Uspekhi* **41**, 469 (1998).
21. P. Natalis, P. Pennetreau, L. Longton, J. E. Collin, *J. Electron Spectrosc. Relat. Phenom.* **27**, 267 (1982).
22. M. W. Schmidt *et al.*, *J. Comput. Chem.* **14**, 1347 (1993).
23. T. Otobe, K. Yabana, J.-I. Iwata, *Phys. Rev. A* **69**, 053404 (2004).
24. A. D. Pradhan, K. P. Kirby, A. Dalgarno, *J. Chem. Phys.* **95**, 9009 (1991).
25. P. Dietrich, P. B. Corkum, *J. Chem. Phys.* **97**, 3187 (1992).
26. D. Pavicic, K. F. Lee, D. M. Rayner, P. B. Corkum, D. M. Villeneuve, *Phys. Rev. Lett.* **98**, 243001 (2007).
27. H. Niikura *et al.*, *Nature* **417**, 917 (2002).
28. Th. Ergler *et al.*, *Phys. Rev. Lett.* **97**, 103004 (2006).
29. S. Baker *et al.*, *Science* **312**, 424 (2006); published online 1 March 2006 (10.1126/science.1123904).
30. M. Kitzler, M. Lezius, *Phys. Rev. Lett.* **95**, 253001 (2005).
31. D. Shafir, Y. Mairesse, D. M. Villeneuve, P. B. Corkum, N. Dudovich, *Nat. Phys.* **5**, 412 (2009).
32. M. H. Alexander, X. Li, R. Liyanage, R. J. Gordon, *Chem. Phys.* **231**, 331 (1998).

33. Supported by the U.S. Air Force Office of Scientific Research, the Alexander von Humboldt Foundation, the Deutsche Forschungsgemeinschaft, the Canadian Institute for Photonics Innovation, and the Natural Sciences and Engineering Research Council of Canada. We thank B. Avery for technical assistance and M. Zimmer for help in preparing some of the graphics.

Supporting Online Material

www.sciencemag.org/cgi/content/full/325/5946/1364/DC1
Materials and Methods
Figs. S1 to S3
References

21 April 2009; accepted 9 July 2009
10.1126/science.1175253

Extremely Efficient Multiple Electron-Hole Pair Generation in Carbon Nanotube Photodiodes

Nathaniel M. Gabor,[1]* Zhaohui Zhong,[2]† Ken Bosnick,[4] Jiwoong Park,[3] Paul L. McEuen[1,2]

We observed highly efficient generation of electron-hole pairs due to impact excitation in single-walled carbon nanotube p-n junction photodiodes. Optical excitation into the second electronic subband E_{22} leads to striking photocurrent steps in the device I-V_{SD} characteristics that occur at voltage intervals of the band-gap energy E_{GAP}/e. Spatially and spectrally resolved photocurrent combined with temperature-dependent studies suggest that these steps result from efficient generation of multiple electron-hole pairs from a single hot E_{22} carrier. This process is both of fundamental interest and relevant for applications in future ultra-efficient photovoltaic devices.

A single-walled carbon nanotube (SWNT), which can be viewed as a rolled sheet of graphene, generates numerous species of one-dimensional charge carriers whose energies (shown in Fig. 1A) are given by:

$$\varepsilon_i(k) = \pm\sqrt{(m_i^* v_F^2)^2 + (\hbar k v_F)^2} \qquad (1)$$

where $v_F = 8 \times 10^5$ m / s is the Fermi velocity of graphene, $\hbar$ is Planck's constant, $\hbar k$ is the carrier momentum along the length of the nanotube, and m_i^* is the effective mass of the ith subband (*1*, *2*). For a semiconducting SWNT, the band-gap energy $E_{11} = 2m_1^* v_F^2$ is the energy required to generate an electron-hole (e-h) pair (Fig. 1B), whereas higher subband energies such as $E_{22} = 2E_{11}$ correspond to excitations with greater effective mass ($m_2^* = 2m_1^*$).

The small Fermi velocity and low dielectric constant in SWNTs suggest that high-energy carriers should efficiently generate e-h pairs. Ef-

ficient e-h pair generation could lead to highly sensitive photodetectors (*3*, *4*), electroluminescent emitters (*5*–*7*), and, particularly, improved-efficiency photovoltaics (*8*–*10*). Multiple electron-hole pair generation could theoretically improve the efficiency of photovoltaic solar cells beyond standard thermodynamic limits (*11*). Recent optical experiments have suggested that such processes occur in semiconductor nanocrystals (*10*, *12*–*14*), but the interpretation of these results is controversial.

We studied electron-hole pair generation in p-n junctions consisting of individual SWNTs in a split-gate field-effect geometry shown schematically in Fig. 1C and as described in previous work (*15*–*17*). Three independent gates, V_1, V_2, and global back gate V_G, allow selective electrostatic doping along the length of the nanotube. By applying voltages of opposite polarities on V_1 and V_2, a p-n junction is realized, which yields a built-in electric field E along the length of the nanotube (Fig. 1B). Photo-generated e-h pairs created in the junction are separated by the built-in potential and accelerated to the device contacts, leading to photocurrent at zero bias.

Devices were placed in an optical scanning microscope setup that combines electronic transport measurements at low temperature with spatially scanned laser illumination (*17*). Figure 1D shows a spatially resolved photocurrent map achieved by recording the current I as a focused laser (λ = 532 nm) is scanned over the device at a source-drain voltage V_{SD} = 0 V and T = 50 K. A photocurrent peak was observed at the location of the p-n junction, with a full width at half maximum of ~700 nm perpendicular to the nanotube, consistent with the size of the excitation beam. We fixed the position of the laser on the p-n junction and measured I-V_{SD} characteristics at various photon energies and T = 60 K for a device of diameter d = 1.4 nm (Fig. 2A). In the absence of light, the dark I-V_{SD} characteristic (black line) demonstrates ordinary p-n junction transport behavior (*15*, *16*): very small current in reverse bias and a threshold for turn-on in forward bias corresponding to the band gap of the SWNT. The illuminated I-V_{SD} characteristic at low photon energy (E_{PHOTON} = 0.75 eV, red curve) also exhibits a standard p-n junction photoresponse: constant photocurrent at reverse and moderate forward bias. At a forward bias equal to the band gap, the built-in potential disappears and the photocurrent goes to zero at the open-circuit voltage (V_{OC} = 0.43 V), which gives the band-gap energy $E_{GAP} = E_{11} \sim eV_{OC}$ in the p-n junction (*18*) (schematic, Fig. 1B).

As the photon energy is increased, we observed a quite different response. The reverse-bias photocurrent increased with increasing photon energy and evolved into a series of steps with increasing reverse bias (Fig. 2A, E_{PHOTON} = 1.24 eV). We present similar results for a device of V_{OC} = 0.3 V in Fig. 2B. Photocurrent steps occurred in reverse bias, and the photocurrent increased linearly with optical power density. We discuss the dependence of these current steps on source-drain bias, photon energy, and temperature.

In Fig. 2A, the spacing of the steps in V_{SD} is $\Delta V_{STEP} \sim 0.4$ V, which is nearly the same as the open-circuit voltage V_{OC} = 0.43 V. Similarly, in Fig. 2B, photocurrent steps occur in intervals ΔV_{STEP} that are approximately equal to the open-circuit voltage, V_{OC} = 0.3 V. To determine the spacing more accurately, we calculated the differential conductance $|dI / dV_{SD}|$ as a function of V_{SD}. Figure 2C shows $|dI / dV_{SD}|$ for SWNT devices of diameters 1.5 nm (orange), 2.0 nm (blue), and 3.6 nm (green). Conductance peaks, corresponding to photocurrent steps, occur at shorter V_{SD} intervals for devices of larger diameter. In Fig. 2D, we plot V_{OC} and ΔV_{STEP} versus SWNT diameter for several devices. The photocurrent step intervals, ΔV_{STEP}, scale inversely with SWNT diameter approximately as ~ 0.66 V-nm / d, shown as a solid line. This result is consistent with the reported dependence of the band-gap energy on diameter d: $E_{11} \sim eV_{OC} \sim 0.7$ eV-nm / d (*1*). We conclude that the spacing ΔV_{STEP} of the photocurrent peaks is equal to the band-gap E_{11} of the SWNT.

Photocurrent spectroscopy measurements show that photocurrent steps occur only for photon energies $E_{PHOTON} > 2E_{11}$. In Fig. 3A, we plot the photocurrent spectra for the device of Fig. 2A at $V_{SD} = V_{OC} / 2$ (slight forward bias) and $V_{SD} = -V_{OC} / 2$ (slight reverse bias). At E_{PHOTON} = 0.81 eV, we observed a narrow spectral peak. Upon normalizing the photon energy by eV_{OC}, we observe that the spectral peak occurs near $E_{PHOTON} \sim 2E_{11}$, which is consistent with optical absorption into the second subband, $E_{22} = 2E_{11}$ (*1*). The extra photocurrent seen at high photon energy ($E_{PHOTON} > 2E_{11}$) corresponds directly to the photocurrent steps in the I-V_{SD} characteristics in Fig. 2A. In Fig. 3B, we observe a similar response for a device of V_{OC} = 0.45 V. We conclude that the photocurrent steps occur only under excitation of second subband electrons e_2 and holes h_2.

The photocurrent steps also occur only at low temperatures. For the device used in Fig. 3B, we show in Fig. 3C the I-V_{SD} characteristics at various temperatures at E_{PHOTON} = 0.95 eV and E_{PHOTON} = 0.76 eV (above and below the spectral peak at $E_{PHOTON} \sim 2E_{11}$). At E_{PHOTON} = 0.95 eV ($E_{PHOTON} > 2E_{11}$), we observed a very strong temperature dependence and clear photocurrent steps below $T \sim 100$ K (Fig. 3C, top). At E_{PHOTON} = 0.76 eV ($E_{PHOTON} < 2E_{11}$), in contrast, the I-V_{SD} characteristics show very weak dependence on temperature, exhibiting no photocurrent steps (Fig. 3C, bottom). In Fig. 3D, we plot the temperature dependence of the reverse ($V_{SD} = -V_{OC} / 2$) and forward ($V_{SD} = V_{OC} / 2$) bias photocurrent. For $E_{PHOTON} > 2E_{11}$, the reverse bias photocurrent (Fig. 3D top) doubles at low temperature, and the forward bias photocurrent shows a similar increase. By extracting the inflection point of the reverse bias data, we assign an onset temperature of T_0 = 90 K, below which photocurrent steps occur. We also measured the

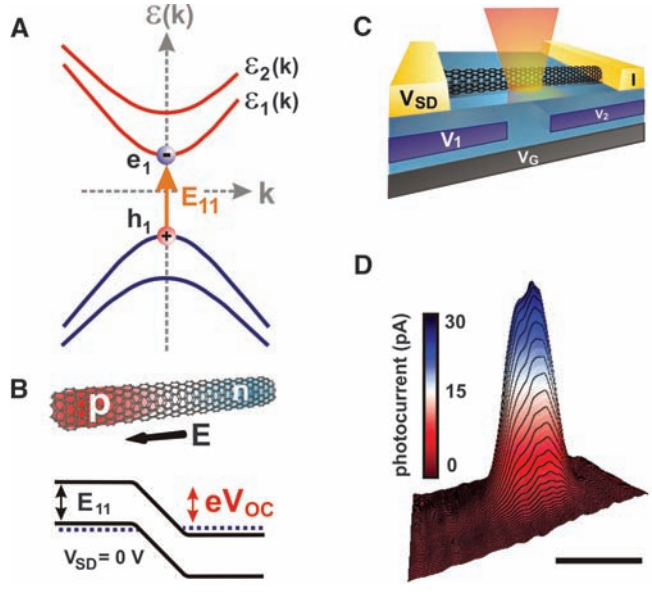

Fig. 1. Band structure, device geometry, and spatial photocurrent of the carbon nanotube p-n junction photodiode. **(A)** Electronic band structure diagram of the carbon nanotube showing electron-hole pair creation into the first subband ε_1 of the nanotube. e_1 labels the electron (blue) and h_1 labels the hole (red) of masses m_1*. **(B)** (Top) Schematic of the carbon nanotube showing p-type (positive, red) and n-type (negative, blue) regions with built-in electric field E. (Bottom) Length-dependent potential energy diagram of p-n junction at V_{SD} = 0 V. Dotted lines represent the electron Fermi energy in the p- and n- type regions of the device, E_{11} is the band-gap energy, and eV_{OC} is the magnitude of the open-circuit voltage potential. **(C)** Experimental schematic of split-gate device under focused optical illumination. **(D)** Spatially resolved photocurrent map at T = 50 K with continuous wave laser excitation λ = 532 nm and optical power density 25 W/cm^2 for a device of diameter d = 1.8 nm ($V_1 = -V_2 = -9.0$ V; $V_G = V_{SD} = 0.0$ V). Scale bar, 1 μm.

[1]Laboratory of Atomic and Solid-State Physics, Cornell University, Ithaca, NY 14853, USA. [2]Center for Nanoscale Systems, Cornell University, Ithaca, NY 14853, USA. [3]Department of Chemistry and Chemical Biology, Cornell University, Ithaca, NY 14853, USA. [4]National Institute for Nanotechnology, National Research Council of Canada, Edmonton, AB T6G 2M9, Canada.

*To whom correspondence should be addressed. E-mail: nmg32@cornell.edu

†Present address: Department of Electrical Engineering and Computer Science, University of Michigan, Ann Arbor, MI 48109, USA.

onset temperature for several devices (Fig. 3D, inset) and observe that T_0 decreases with diameter. Thus, these steps occur only for photon energies larger than E_{22} and below a characteristic temperature that depends on the SWNT diameter.

We attribute these photocurrent steps to highly efficient e-h creation by high-energy charge carriers in the second SWNT subband. In the e-h generation process requiring the lowest excess energy, the excess rest mass energy of the second subband carriers ($m_2^* v_F^2$) is combined with the kinetic energy of the electric field to create an ε_1 carrier plus electron-hole pairs (Fig. 4, A and B)

$$e_2 + K_e(x) \rightarrow e_1 + n(e_1 + h_1) \quad (2a)$$

and equivalently for holes

$$h_2 + K_h(x) \rightarrow h_1 + n(e_1 + h_1) \quad (2b)$$

The integer $n = 1, 2, 3...$ indicates the number of e-h pairs produced in the final state of the generation process. The intermediate states of Eq. 2 may involve an ε_2 carrier undergoing several impact excitation events or a single relaxation event that results in numerous e-h pairs. The kinetic energy available to electrons (K_e) and holes (K_h) created at a position x along the p-n junction of length L is given by

$$K_e(x) = e\phi(x) \quad (3a)$$

$$K_h(x) = e\phi_0 - e\phi(x) \quad (3b)$$

where $e\phi(x)$ is the electric potential energy and $e\phi_0 = e\phi(L) - e\phi(0) = E_{11} - eV_{SD}$ is the total potential energy drop across the p-n junction. The potential energy drop can be tuned by changing V_{SD}. At the open-circuit voltage, $V_{SD} = V_{OC} \sim E_{11} / e$, the total potential energy drop is zero, whereas at $V_{SD} = 0$, the total potential energy available along the entire junction is E_{11}.

This model makes a number of predictions that can be compared to experiment. First, the amount of kinetic energy gained by a carrier in the p-n junction depends strongly on its initial location (Fig. 4, A and B). For carriers excited at the edge of the junction, either the electron or the hole picks up the entire potential energy of the junction while the other is unaffected (Fig. 4A). For the electron and hole created at the center, each picks up only half of the junction's potential energy (Fig. 4B). The threshold for impact excitation will depend on the location of the photoexcitation.

We used scanning photocurrent microscopy to test this conjecture. In Fig. 4D, we plot photocurrent profiles for a device of $V_{OC} = 0.45$ V taken by scanning the laser ($\lambda = 676$ nm) along the length of the nanotube at various V_{SD} values. At $V_{SD} = 0.35$ V, we observed a flat photocurrent profile that extends across the entire p-n junction with a constant value of ~10 pA. Such standard behavior does not include the effects of impact excitation. At $V_{SD} = V_{OC} / 2 = 0.225$ V, the photocurrent profile exhibits a double-peaked structure with photocurrent maxima occurring at the edges of the p-n junction, corresponding to the case shown in Fig. 4A. When the bias voltage reaches $V_{SD} = 0$ V, an additional sharp increase occurs at the center of the device, corresponding to Fig. 4B. In reverse bias, the photocurrent peaks at the edges catch up to the center peak (at $V_{SD} = -V_{OC}$) until finally, at high reverse bias, the center peak again dominates over the side peaks.

To explore this spatial dependence in detail, we first fixed the laser on the edge of the p-n junction (Fig. 4E). The first photocurrent step occurs in forward bias at $V_{SD} \sim 0.25$ V. The first photocurrent step in forward bias corresponds to the edge peaks of the double-peaked structure in the spatial photocurrent profile at low temperature (Fig. 4C). The second step is observed at $V_{SD} \sim -0.20$ V, with a spacing between photocurrent steps $\Delta V_{STEP} \sim V_{OC} = E_{11}$.

The photocurrent voltage threshold for the first step highlights a key feature of the e-h generation process. When the laser is fixed at the edge of the p-n junction, electron-hole pair creation first occurs in forward bias at $V_{SD} = \frac{1}{2} E_{11} / e = V_{OC} / 2$. The electric field need only provide kinetic energy of $\frac{1}{2} E_{11}$ while the remaining energy is provided by the conversion of rest mass energy (or equivalently by excess subband energy), as indicated in Eq. 2.

For comparison, we next show I-V_{SD} characteristics with the laser fixed on the center of the p-n junction (Fig. 4F). Because electrons e_2 and holes h_2 start at the center of the p-n junction and gain only half of the electric potential energy, the applied voltage V_{SD} threshold for electron-hole pair production is doubled. Indeed, we observed the first photocurrent step near $V_{SD} = 0$ V and additional steps in reverse bias at V_{SD} intervals of $2V_{OC}$. At higher kinetic energies, additional e-h pair production requires an additional combined energy of $2E_{11}$ from the electric field (E_{11} for each of the electron and hole) and leads to photocurrent steps at larger voltage intervals of $2V_{OC}$. This response is consistent with the e-h pair production process of Eq. 2: The onset voltage threshold and voltage spacing for additional steps depend strongly on the initial location of the photoexcited carrier.

The extremely high efficiency of the $e_2 + K_e \rightarrow e_1 + n(e_1 + h_1)$ process is an unexpected

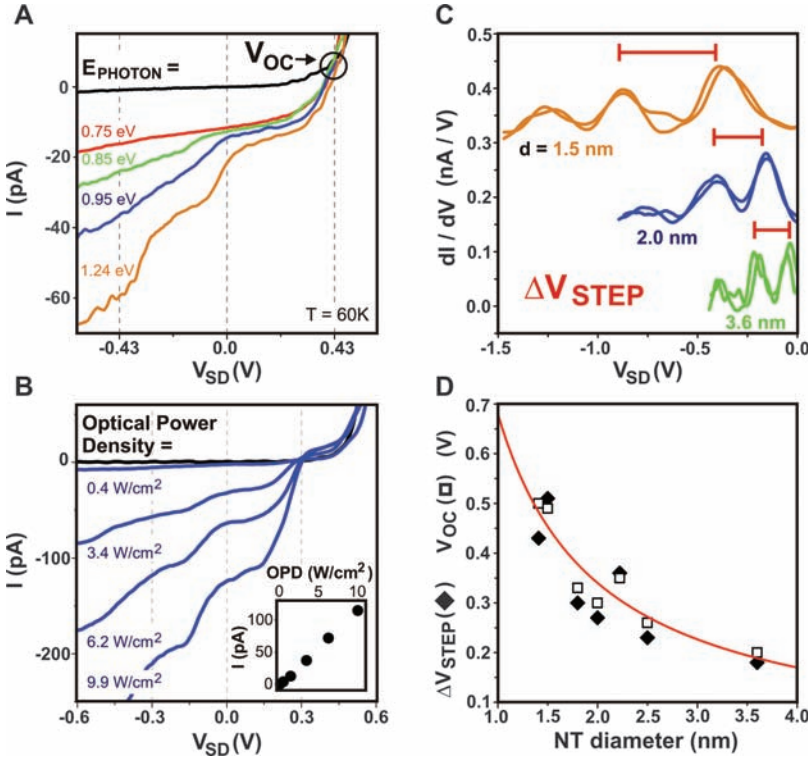

Fig. 2. I-V_{SD} photocurrent characteristics, diameter dependence of the open-circuit voltage V_{OC}, and photocurrent step interval ΔV_{STEP} in carbon nanotube p-n junction photodiodes. (**A**) I-V_{SD} characteristics at $T = 60$ K for SWNT with diameter $d = 1.4$ nm at various photon energies (labeled), $V_1 = -V_2 = 7.5$ V, $V_G = 1.2$ V, and optical power density 25 W/cm^2. (**B**) I-V_{SD} characteristics at $T = 10$ K and $E_{PHOTON} = 0.79$ eV for a device of $d = 2.0$ nm and open-circuit voltage $V_{OC} = 0.3$ V at several optical power densities (labeled) up to 10 W/cm^2. (Inset) Photocurrent at $V_{SD} = 0$ V versus optical power density. (**C**) Reverse bias differential conductance $|dI / dV_{SD}|$ (from I-V_{SD} data) at low temperatures for devices with various diameters (labeled, offset by intervals of 1.5 nA/V) and multiple optical power densities [normalized and rescaled for comparison to the bottom device by factors ×6 (orange), ×3 (blue), and ×1 (green) at $\lambda = 1420$ nm (orange) and $\lambda = 1560$ nm (blue and green)]. ΔV_{STEP} labels the V_{SD} spacing between $|dI / dV_{SD}|$ peaks. (**D**) ΔV_{STEP} and V_{OC} plotted against nanotube (NT) diameter for several devices.

result. Normally, relaxation mechanisms, such as optical phonon emission, are very efficient for relaxing hot carriers, including those in the first subband of SWNTs (*17*, *19*–*21*). We do not know why the $e_2 \rightarrow e_1$ process reported here is different. However, other phonons may be important in reducing e-h pair generation at elevated temperatures, as seen in Fig. 4. The thermal energy at the onset temperature is comparable to

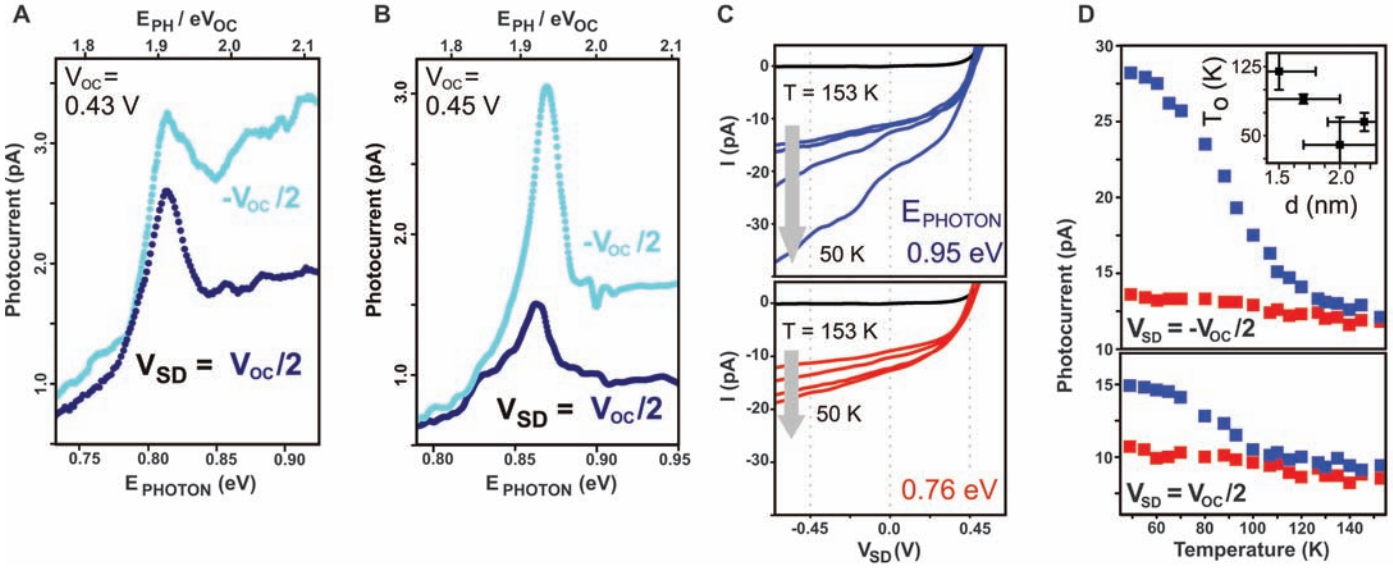

Fig. 3. Photocurrent spectroscopy and temperature dependence of photocurrent in the SWNT p-n junction. (**A**) Photocurrent spectra for device of Fig. 2A measured at $V_{SD} = V_{OC} / 2 = 0.225$ V (navy blue), and $V_{SD} = -V_{OC} / 2 = -0.225$ V (cyan), OPD = 3 W/cm^2. Top axis normalized by eV_{OC}. (**B**) Photocurrent spectra for another device ($d = 1.7$ nm, $V_{OC} = 0.45$ V, $V_1 = -V_2 = 6.0$ V, $V_G = 1.5$ V, $T = 49$ K), measured at $V_{SD} = V_{OC} / 2 = 0.225$ V (navy blue), and $V_{SD} = -V_{OC} / 2 = -0.225$ V (cyan), OPD = 3 W/cm^2. Top axis normalized by eV_{OC}. (**C**) (Top) I-V_{SD} characteristics for the device in Fig. 3B measured at photon energy $E_{PHOTON} = 0.95$ eV (blue) at various temperatures (descending in direction of arrow $T = 153$, 127, 107, 50 K), OPD = 25 W/cm^2. (Bottom) I-V_{SD} characteristics measured for the same device at photon energy $E_{PHOTON} = 0.76$ eV (red) over the same temperature range. (**D**) (Top) Temperature dependence of reverse bias ($V_{SD} = -V_{OC} / 2 = -0.225$ V) photocurrent at various temperatures for photon energies $E_{PHOTON} = 0.76$ eV (red) and $E_{PHOTON} = 0.95$ eV (blue). (Bottom) Temperature dependence of forward bias photocurrent ($V_{SD} = +V_{OC} / 2 = 0.225$ V). (Top inset) Photocurrent step onset temperature T_0 versus diameter for several devices.

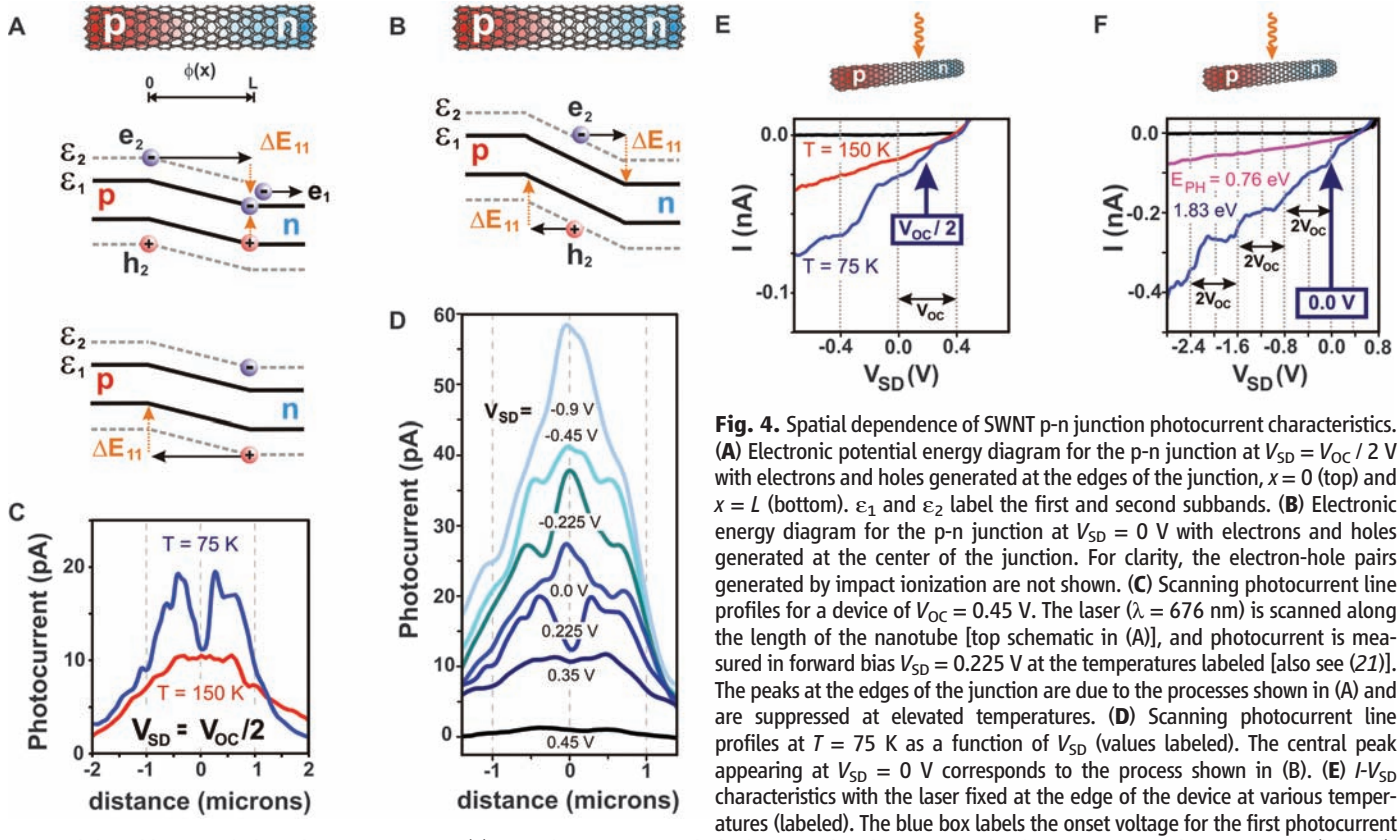

Fig. 4. Spatial dependence of SWNT p-n junction photocurrent characteristics. (**A**) Electronic potential energy diagram for the p-n junction at $V_{SD} = V_{OC} / 2$ V with electrons and holes generated at the edges of the junction, $x = 0$ (top) and $x = L$ (bottom). ε_1 and ε_2 label the first and second subbands. (**B**) Electronic energy diagram for the p-n junction at $V_{SD} = 0$ V with electrons and holes generated at the center of the junction. For clarity, the electron-hole pairs generated by impact ionization are not shown. (**C**) Scanning photocurrent line profiles for a device of $V_{OC} = 0.45$ V. The laser ($\lambda = 676$ nm) is scanned along the length of the nanotube [top schematic in (A)], and photocurrent is measured in forward bias $V_{SD} = 0.225$ V at the temperatures labeled [also see (*21*)]. The peaks at the edges of the junction are due to the processes shown in (A) and are suppressed at elevated temperatures. (**D**) Scanning photocurrent line profiles at $T = 75$ K as a function of V_{SD} (values labeled). The central peak appearing at $V_{SD} = 0$ V corresponds to the process shown in (B). (**E**) I-V_{SD} characteristics with the laser fixed at the edge of the device at various temperatures (labeled). The blue box labels the onset voltage for the first photocurrent step, and dotted lines mark the voltage spacing V_{OC}. (**F**) I-V_{SD} characteristics with the laser fixed at the center of the device at various photon energies (labeled).

the radial breathing mode (RBM) energy $E_{RBM} \sim 7meV / d$ nm (*1*, *2*) and other low-energy radial phonons. Indeed, recent optical measurements of the relaxation process $E_{22} \rightarrow E_{11}$ have suggested strong exciton-phonon coupling to the SWNT radial breathing mode at room temperature (*22*). Although the low temperature onset of impact excitation is comparable to the freeze-out of RBM phonons ($T < E_{RBM} / k_B \sim 80$ K), other processes may be responsible.

The impact excitation process $e_2 + K_e \rightarrow e_1 + n(e_1 + h_1)$ differs strongly from impact ionization observed in traditional semiconductors in two important ways. First, no avalanche breakdown behavior is observed here because hot ε_2 carriers create ε_1 carriers, which do not undergo additional multiplication at low reverse bias (see SOM text). Second, the process observed here is extremely efficient, occurring as soon as it is energetically allowed. In standard semiconductors, competing loss mechanisms restrict impact excitation to extremely large biases (*18*).

These results also differ strongly from previous theory and experiments on SWNTs. Perebeinos *et al*. (*23*) calculated that single-particle impact excitation in SWNTs should be highly efficient, but only in the third subband and higher because of momentum conservation transverse to the tube axis. We observed a highly efficient process in the second subband, suggesting that either other carriers or phonons are involved to conserve momentum. Earlier experiments on SWNT transistors attributed bright electroluminescence (*5*–*7*) and avalanche breakdown (*24*) (see SOM text) to electron-hole generation by impact excitation, but as with traditional semiconductors, these processes were only observed at large biases, and the importance of the subband index was not discussed.

The e-h pair creation process observed here may make possible increased power conversion efficiency in future photovoltaic devices. The standard limit of photovoltaic efficiency, first established by Shockley and Queisser (*11*), is set by the conversion of a single photon into a single e-h pair. In the SWNT p-n junction, a single photon with energy $E_{PHOTON} > E_{22}$ is converted into multiple e-h pairs, leading to enhanced photocurrent and increased efficiency. Evidence for a related process, known as multiple exciton generation (MEG) (*10*, *12*–*14*), has been observed in various semiconductor nanocrystals, but these observations remain controversial, and improved photovoltaic device behavior has not been demonstrated. The results presented here clearly show that multiple e-h pairs can be generated and collected in a nanotube p-n junction. Although implementation of devices exploiting e-h pair generation into photovoltaic cells will require substantial future effort, the process observed here has substantial implications for such technology and represents a very important step toward ultra-efficient photovoltaic devices with power conversion efficiency exceeding the Shockley-Queisser limit.

References and Notes

1. R. Saito, G. Dresselhaus, M. S. Dresselhaus, *Physical Properties of Carbon Nanotubes* (Imperial College, London, 1998).
2. P. Avouris, Z. Chen, V. Perebeinos, *Nat. Nanotechnol.* **2**, 605 (2007).
3. O. Hayden, R. Agarwal, C. M. Lieber, *Nat. Mater.* **5**, 352 (2006).
4. C. Yang, C. J. Barrelet, F. Capasso, C. M. Lieber, *Nano Lett.* **6**, 2929 (2006).
5. J. A. Misewich *et al*., *Science* **300**, 783 (2003).
6. J. Chen *et al*., *Science* **310**, 1171 (2005).
7. L. Marty *et al*., *Phys. Rev. Lett.* **96**, 136803 (2006).
8. B. Tian *et al*., *Nature* **449**, 885 (2007).
9. J. U. Lee, *Appl. Phys. Lett.* **87**, 073101 (2005).
10. R. D. Schaller, V. I. Klimov, *Phys. Rev. Lett.* **92**, 186601 (2004).
11. W. Shockley, H. J. Queisser, *J. Appl. Phys.* **32**, 510 (1961).
12. R. J. Ellingson *et al*., *Nano Lett.* **5**, 865 (2005).
13. J. Kim *et al*., *Appl. Phys. Lett.* **92**, 031107 (2008).
14. R. D. Schaller, V. M. Agranovich, V. I. Klimov, *Nat. Phys.* **1**, 189 (2005).
15. J. U. Lee, P. Gipp, C. M. Heller, *Appl. Phys. Lett.* **85**, 145 (2004).
16. K. Bosnick, N. M. Gabor, P. L. McEuen, *Appl. Phys. Lett.* **89**, 163121 (2006).
17. Materials and methods are available as supporting material on *Science* Online.
18. S. M. Sze, *Physics of Semiconductor Devices* (Wiley, London, ed. 2, 1981).
19. E. Pop *et al*., *Phys. Rev. Lett.* **95**, 155505 (2005).
20. J. Y. Park *et al*., *Nano Lett.* **4**, 517 (2004).
21. Z. Yao, C. L. Kane, C. Dekker, *Phys. Rev. Lett.* **84**, 2941 (2000).
22. C. Manzoni *et al*., *Phys. Rev. Lett.* **94**, 207401 (2005).
23. V. Perebeinos, P. Avouris, *Phys. Rev. B* **74**, 121410 (2006).
24. A. Liao, Y. Zhao, E. Pop, *Phys. Rev. Lett.* **101**, 256804 (2008).

25. We thank R. Ilic and J. Kinder for useful discussions. This work was supported by the NSF through the Center for Nanoscale Systems and by the Microelectronics Advanced Research Corporation Focused Research Center on Materials, Structures, and Devices. Sample fabrication was performed at the Cornell Nanoscale Science and Technology Facility, a National Nanotechnology Infrastructure Network node, funded by NSF.

Supporting Online Material

www.sciencemag.org/cgi/content/full/325/5946/1367/DC1
Materials and Methods
SOM Text
Figs. S1 to S3
References

11 May 2009; accepted 13 July 2009
10.1126/science.1176112

Underplating in the Himalaya-Tibet Collision Zone Revealed by the Hi-CLIMB Experiment

John Nábělek,[1]* György Hetényi,[2]† Jérôme Vergne,[2]‡ Soma Sapkota,[3] Basant Kafle,[3]§ Mei Jiang,[4] Heping Su,[4] John Chen,[5] Bor-Shouh Huang,[6] the Hi-CLIMB Team‖

We studied the formation of the Himalayan mountain range and the Tibetan Plateau by investigating their lithospheric structure. Using an 800-kilometer-long, densely spaced seismic array, we have constructed an image of the crust and upper mantle beneath the Himalayas and the southern Tibetan Plateau. The image reveals in a continuous fashion the Main Himalayan thrust fault as it extends from a shallow depth under Nepal to the mid-crust under southern Tibet. Indian crust can be traced to 31°N. The crust/mantle interface beneath Tibet is anisotropic, indicating shearing during its formation. The dipping mantle fabric suggests that the Indian mantle is subducting in a diffuse fashion along several evolving subparallel structures.

The collision of the Indian tectonic plate with Eurasia is the primary force behind the rise of the Himalayan mountain range and the uplift of the Tibetan Plateau. The Indian lithosphere has been underthrusting beneath Tibet since the closing of the Tethys Sea in the early Tertiary, and the mountain-building deformation front has moved southward from the initial collision contact at the Yarlung Tsangpo Suture by processes that transfer Indian crust to the overriding plate. Seismological studies [such as (*1*–*4*)] have shown that the Indian plate continues to underthrust southern Tibet at least up to the south Lhasa Block, but its northern limit and geometry are still uncertain (*5*).

Here we present a high-resolution continuous cross section of lithospheric interfaces through the Himalayas and the southern half of the Tibetan Plateau constructed from seismological data acquired in 2002–2005 by the project Hi-CLIMB

[1]College of Oceanic and Atmospheric Sciences, Oregon State University, Corvallis, OR 97331, USA. [2]Laboratoire de Géologie, École Normale Supérieure, CNRS-UMR 8538, 24 Rue Lhomond, 75005 Paris, France. [3]National Seismological Center, Department of Mines and Geology, Kathmandu, Nepal. [4]Institute of Geology, Chinese Academy of Geological Sciences, Beijing, People's Republic of China (PRC). [5]Institute of Theoretical and Applied Geophysics, Peking University, Beijing, PRC. [6]Institute of Earth Sciences, Academia Sinica, Taipei, Taiwan.

*To whom correspondence should be addressed. E-mail: nabelek@coas.oregonstate.edu
†Present address: Earth Sciences Department, ETH Zurich, 8092 Zurich, Switzerland.
‡Present address: Ecole et Observatoire des Sciences de la Terre, CNRS-UMR 7516, 5 rue René Descartes, 67084 Strasbourg, France.
§Present address: Alberta Geological Survey, 4999-98 Avenue, Edmonton, Alberta T6B 2X3, Canada.
‖All additional authors with their affiliations appear at the end of this paper.